

Fig. 2. (a) Voltage transfer characteristic of two Schmitt triggers designed to exhibit hysteresis at different supply voltages,  $V_{DDH}$ , and (b) their maximum absolute gain as a function of the supply voltage  $V_{DD}$ .

where the current scaling factor  $I_N$ , which represent the transistor strength, is given by

$$I_N = \mu_N \cdot n_N \cdot C'_{ox} \cdot \phi_t^2 \cdot \frac{W}{L} \cdot e^{-\frac{|V_{T0N}|}{n_N \phi_t} + 1}. \quad (2)$$

$W/L$  is the aspect ratio,  $\mu_N$  is the mobility,  $C'_{ox}$  is the oxide capacitance per unit area,  $\phi_t$  is the thermal voltage,  $V_{T0N}$  is the threshold voltage and  $n_N$  is the slope factor.

G, S, D and B are the gate, source, drain, and bulk nodes, respectively. The expression for the pMOS current is obtained from (1) changing  $V_{SB}$  by  $V_{BS}$ ,  $V_{DB}$  by  $V_{BD}$  and  $V_{GB}$  by  $V_{GB}$ . The expression for the current strength of the pMOS transistor is the same as (2), using the pMOS parameters.

All transistors of the Schmitt trigger are such that every pMOS has the same current strength as its symmetric nMOS, that is,  $I_{N0} = I_{P0} = I_0$ ,  $I_{N1} = I_{P1} = I_1$ ,  $I_{N2} = I_{P2} = I_2$  and  $n_N = n_P = n$ .

As shown in [15], the minimum supply voltage to obtain hysteresis in a Schmitt trigger with balanced pMOS and nMOS subcircuits is given by

$$V_{DDH} \approx 2\phi_t \ln \left[ n \left( 1 + \frac{I_0}{I_2} \right) \left( 1 + \frac{I_1}{I_0} + \frac{I_2}{I_0} \right) - \frac{I_1}{I_0} \right]. \quad (3)$$

Figures 2a and 2b show the voltage transfer characteristic and the maximum absolute gain, respectively, of two Schmitt triggers, one with  $V_{DDH} = 100$  mV and the other with  $V_{DDH} = 150$  mV.

Note that the maximum absolute gain increases until hysteresis appears at a certain level, herein  $V_{DDH}$ . It can be seen that, for the same supply voltage  $V_{DD}$ , the Schmitt trigger that exhibits hysteresis at a lower voltage consistently has a higher maximum absolute gain. The value of  $V_{DDH}$  depends on the values of  $I_0$ ,  $I_1$  and  $I_2$ , and thus is chosen during the design.  $I_0 = 70$  nA,  $I_1 = 2.8$  nA and  $I_2 = 25$  nA give  $V_{DDH} = 100$  mV, while  $I_0 = 46$  nA,  $I_1 = 7.4$  nA and  $I_2 = 4.6$  nA give  $V_{DDH} = 150$  mV.

On the other hand, Figures 3a and 3b let us compare the gain of a CMOS inverter to the gain of a Schmitt trigger, as a

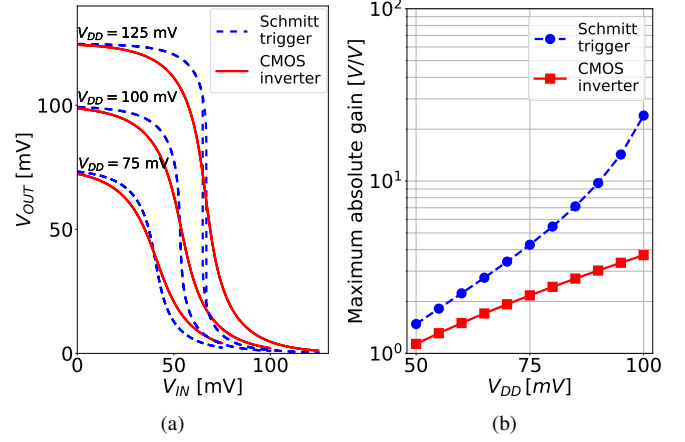


Fig. 3. (a) Voltage transfer characteristic of a Schmitt trigger with  $V_{DDH} = 100$  mV and of a CMOS inverter and (b) their maximum absolute gain as a function of the supply voltage  $V_{DD}$ .

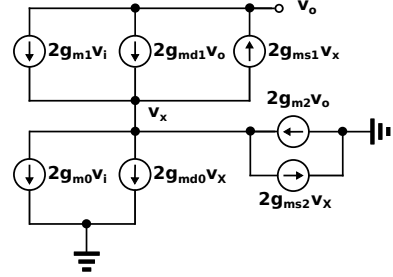


Fig. 4. Six transistor Schmitt trigger circuit low-frequency small-signal equivalent model for  $V_I = V_O = V_{DD}/2$ .

function of  $V_{DD}$ . The Schmitt trigger exhibits a much higher maximum absolute gain. Thus, for a given supply voltage it is possible to design a Schmitt trigger with maximum absolute gain much higher than that of a CMOS inverter.

The equivalent small-signal model of the Schmitt trigger in Fig. 4, looks like the nMOS network small-signal model, but all transconductance values are doubled. The numbers in the subscripts of the transconductances refer to the number of the transistor indicated in Fig. 1. This small signal model holds, provided that the supply voltage is lower than  $V_{DDH}$ , preventing the hysteresis from appearing. Later in Section V, the results will show that the performance of the oscillator is degraded for supply voltages above  $V_{DDH}$ .

The Schmitt trigger can be represented by an equivalent transconductance  $G_m$  and an equivalent output conductance  $G_o$ . These two parameters are expressed in terms of  $g_{mg}$ ,  $g_{ms}$  and  $g_{md}$  in Appendix B.

Lastly, the Schmitt trigger voltage gain is expressed as

$$A = \frac{v_o}{v_i} \Big|_{V_I=V_O=V_{DD}/2} = -\frac{G_m}{G_o}. \quad (4)$$

The voltage gain is a function of the supply voltage  $V_{DD}$ , the ratios  $I_1/I_0$  and  $I_2/I_0$ , and the slope factor of nMOS and pMOS devices  $n_N$  and  $n_P$  (considered equal for the sake of simplicity, without loss of generality, thus:  $n = n_N = n_P$ ). The absolute voltage gain increases with the transconductance

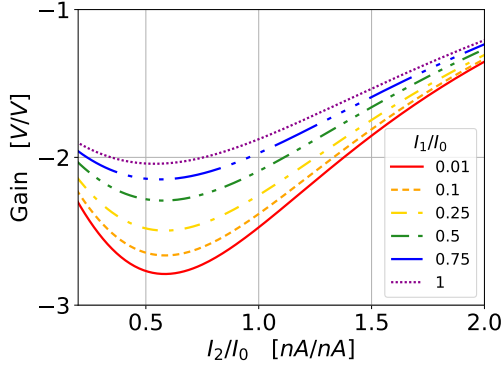


Fig. 5. Voltage gain as a function of  $I_1/I_0$  and  $I_2/I_0$  given by (4), with  $n = 1.3$  and  $V_{DD} = 60 \text{ mV}$ , based on [13].

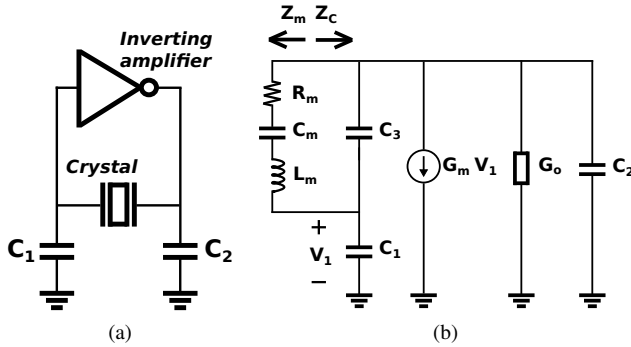


Fig. 6. Pierce crystal oscillator (a) circuit schematic and (b) impedance equivalent model.

$G_m$ , and the latter should be sufficient to compensate for all losses to enable oscillation.

Figure 5 shows the dependence of the voltage gain on  $I_2/I_0$ , for constant values of  $I_1/I_0$  and supply voltage  $V_{DD} = 60 \text{ mV}$ . We have chosen this ultra-low-voltage to explore the frontier of the design space. A practical ultra-low-voltage complex circuit should operate with a minimum supply of  $100 \text{ mV}$  as explained in the introduction. For values of  $I_2/I_0$  close to  $0.5$ , independently of the ratio  $I_1/I_0$ , the maximum absolute gain is reached. Therefore,  $I_2/I_0 = 0.5$  is chosen. On the other hand, the lower the ratio  $I_1/I_0$ , the larger the magnitude of the voltage gain.  $I_1/I_0 = 0.25$  is chosen for the sake of layout simplicity. In this case, the voltage gain is  $A = -2.48 \text{ V/V}$ .

As a consequence, after  $V_{DD}$ ,  $I_1/I_0$  and  $I_2/I_0$  have been selected and  $n$  is given by the process chosen,  $G_m$  and  $G_o$  can be expressed only in terms of the current strength  $I_0$ .

### III. DESIGN OF CRYSTAL OSCILLATORS BASED ON SCHMITT TRIGGER

A schematic of a Pierce oscillator [11], consisting of a quartz crystal connected to an amplifier and two functional capacitors  $C_1$  and  $C_2$ , can be seen in Fig. 6a.

Fig. 6b shows the equivalent impedance model of the circuit in Fig. 6a. On the left side, the series association of  $R_m$ ,  $C_m$  and  $L_m$  represent the crystal motional impedance. On the right side,  $Z_C$  represents the small signal model of the rest of the circuit connected in parallel to the crystal and

TABLE I  
CRYSTALS AND OTHER DISCRETE COMPONENTS OF THE OSCILLATORS.

Parameter	Oscillator A	Oscillator B
Crystal part number	ABS07W-32.768kHz-D1	AB38T-32.768kHz-12.5pF-E-7
$f$ [kHz]	32.768	32.768
$C_m$ [fF]	4.68	3.5
$L_m$ [H]	5 048.571	6 740.193
$R_m$ [k $\Omega$ ]	38.194	15.419
$Q$	27 214	90 000
$C_L$ [pF]	3	12.5
$C_1 = C_2$ [pF]	6	25
$C_3$ [pF]	1.15	1.60
$R_F$ [G $\Omega$ ]	5	5

also the crystal parallel capacitance  $C_3$ .  $G_m$  and  $G_o$  are the transconductance and the output conductance of the inverting amplifier, respectively.

The key auxiliary parameters and equations of this circuit, based on [11], are summarized in Appendix A.

Two oscillators, A and B, were designed. Oscillator A includes a crystal suitable for smaller external capacitors. On the other hand oscillator B uses a crystal with a lower motional resistance,  $R_m$ , providing a larger quality factor  $Q$ .

Table I summarizes all parameters related to the two crystals, that is, resonance frequency  $f$ , motional capacitance  $C_m$ , motional inductor  $L_m$ , motional resistance  $R_m$ , quality factor  $Q$ , the load capacitance  $C_L$  ( $C_1$  in series with  $C_2$ ) and the parallel capacitance  $C_3$ . Here,  $C_1 = C_2 = 2 \times C_L$  for simplicity. A feedback resistor  $R_F$  is connected in parallel to the crystal for biasing purposes.

A Schmitt trigger is used as the inverting amplifier of the Pierce oscillator. As a rule of thumb [16], the transconductance  $G_m$  is designed to be  $3 \times G_{m_{crit}}$ , with  $G_{m_{crit}}$  the critical value of the transconductance to enable oscillation. In addition, the transconductance  $G_m$  is further increased to compensate losses in  $G_o$ . With  $C_1 = C_2$ ,  $\Delta G_m = G_o$  as shown in Appendix A. Thus,

$$G_m = 3 \times G_{m_{crit}} + G_o. \quad (5)$$

From (4) and (5),

$$G_m = \frac{3 \times G_{m_{crit}}}{1 + 1/A}. \quad (6)$$

On the other hand,  $G_m$  can be expressed only in terms of the design parameters  $I_0$ ,  $I_1$ ,  $I_2$  and  $V_{DD}$ , according to (15) found in Appendix B. Figure 7 shows the dependence of  $I_0$  on the transconductance  $G_m$ , for  $I_1/I_0 = 0.25$  and  $I_2/I_0 = 0.5$  according to the design in Section II. As a consequence,  $I_0$  is determined for each oscillator, with  $G_{mA} = 561 \text{ nS}$  and  $G_{mB} = 2 612 \text{ nS}$  according to the values in Table I.

Table II summarizes all parameters related to both Schmitt trigger circuits, that is, the supply voltage  $V_{DD}$ , current strengths  $I_0$ ,  $I_1$  and  $I_2$ , current consumption  $I_{DD}$ , voltage gain  $A$ , transconductance  $G_m$ , output conductance  $G_o$  and dimensions of all the transistors involved.

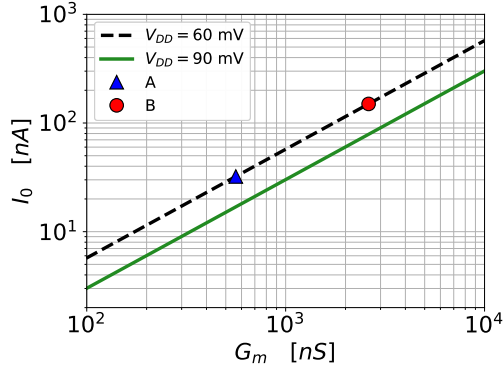


Fig. 7. The required current strength parameter  $I_0$  as a function of the transconductance  $G_m$  in (15), for supply voltages 60 mV and 90 mV.  $G_m$  also fulfills (6) for each oscillator, A or B, with  $G_{m,A} = 561$  nS (blue triangle) and  $G_{m,B} = 2\,612$  nS (red circle).

TABLE II  
OPERATING POINT AND TRANSISTOR DIMENSIONS OF BOTH SCHMITT TRIGGER CIRCUITS.

	Parameter	A	B
Design parameters	$V_{DD}$ [mV]	60	60
	$I_0$ [nA]	32.2	150
	$I_1$ [nA]	8.05	37.5
	$I_2$ [nA]	16.1	74.9
Performance parameters	$I_{DD}$ [nA]	27.7	129
	$G_m$ [nS]	561	2\,612
	$G_o$ [nS]	226	1\,053
	$A$ [V/V]	-2.48	-2.48
Transistor dimensions	$L_{N,P}$ [ $\mu\text{m}$ ]	1.08	1.08
	$W_{N0}$ [ $\mu\text{m}$ ]	$8 \times 5.1$	$16 \times 11$
	$W_{P0}$ [ $\mu\text{m}$ ]	$8 \times 53$	$16 \times 120$
	$W_{N1}$ [ $\mu\text{m}$ ]	$2 \times 5.1$	$4 \times 11$
	$W_{P1}$ [ $\mu\text{m}$ ]	$2 \times 53$	$4 \times 120$
	$W_{N2}$ [ $\mu\text{m}$ ]	$4 \times 5.1$	$8 \times 11$
	$W_{P2}$ [ $\mu\text{m}$ ]	$4 \times 53$	$8 \times 120$

Lastly, a couple of assumptions remain to be verified. Equation (9), with  $C_1 = C_2$ , becomes  $2\omega R_m C_3(1 + 2C_3/C_1) \ll 1$ , which holds for oscillators A and B, given that  $0.035 \ll 1$  and  $0.011 \ll 1$ , respectively. Also, in Appendix A it is stated that even though  $G_m$  is 3 times the critical value, it would still be well below  $G_{mopt}$  in (10). Since  $G_{mopt,A} = 8\,915$  nS and  $G_{mopt,B} = 90\,719$  nS, it holds that  $G_m \ll G_{mopt}$ .

To complete the understanding on the advantages of using a Schmitt trigger instead of a CMOS inverter, an oscillator based on a CMOS inverter and using the crystal in oscillator A, was designed. For comparison purposes the same unitary transistors are used and  $V_{DD} = 60$  mV. Figure 8 shows the simulation results of output voltage amplitude of the oscillators based on a CMOS inverter and based on a Schmitt trigger. The results in the FS and SF corners show that the CMOS inverter has a lot more variability than the Schmitt trigger. In fact, the oscillator based on a CMOS inverter in the FS corner does not start with less than 80 mV supply and in the SF corner with less than 75 mV supply. Furthermore, the

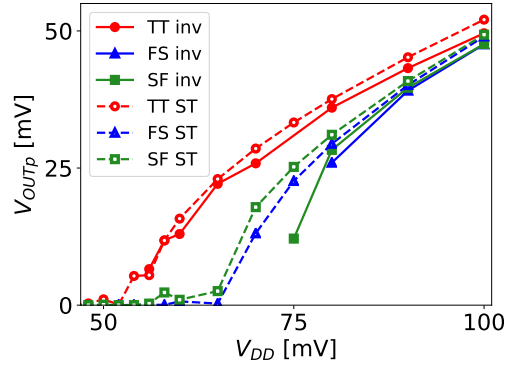


Fig. 8. Simulation results of the output peak amplitude of an oscillator based on a CMOS inverter and an oscillator based on a Schmitt trigger, versus the supply voltage.

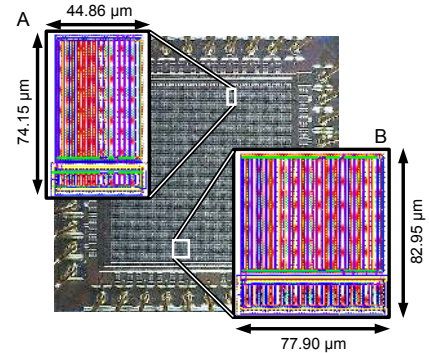


Fig. 9. Microphotograph of the fabricated IC, showing circuits A and B, which are the two Schmitt trigger circuits referred to in this paper.

simulation results also show that the standard deviation of the oscillation frequency is 0.16 Hz and 0.53 Hz in the case of the Schmitt trigger and the CMOS inverter, respectively.

The fact that the oscillators in the FS and SF corners do not start, together with the higher standard deviation of the oscillation frequency, make the oscillator based on a CMOS inverter unsuitable at supply voltages as low as 60 mV.

#### IV. MEASUREMENT RESULTS FOR THE SCHMITT TRIGGER AS AN AMPLIFIER

A test chip including circuits A and B was designed and fabricated in a 130 nm technology. A microphotograph of one die is shown in Fig. 9. The actual position of these circuits in the die and their dimensions were drawn and superimposed. The layout of each circuit is also depicted. The area occupied by circuit A is  $44.86 \mu\text{m} \times 74.15 \mu\text{m}$ . Circuit B occupies a larger area ( $77.90 \mu\text{m} \times 82.95 \mu\text{m}$ ), which is related to the need for a higher current drive.

The voltage transfer characteristic of the Schmitt trigger was measured as a function of the supply voltage by means of a semiconductor parameter analyzer (HP4156). Figs. 10a and 10b, show the voltage transfer characteristic of circuits A and B, respectively, and the simulation results are also shown.

The maximum absolute gains for circuits A and B were extracted from the voltage transfer characteristic measurements and simulations, as shown in Fig. 11a. The estimated

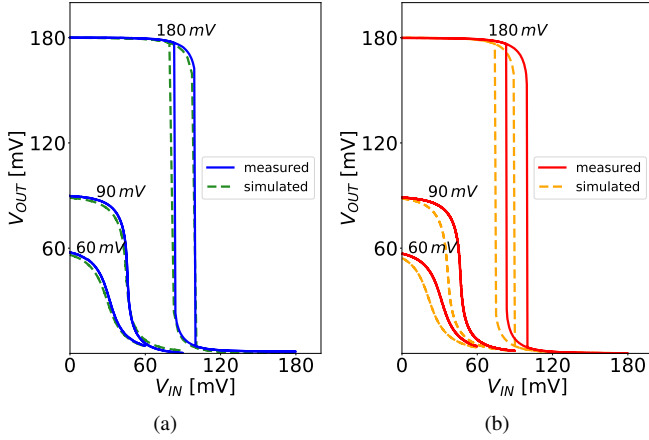


Fig. 10. Simulation and measurement results for the Schmitt trigger voltage transfer characteristic. Results for different supply voltages are displayed for both circuits, (a) A and (b) B.

curve was calculated using (4), which is why the results are expected to be the same for circuits A and B, since they were designed to achieve the same gain. Accordingly, the simulation results for the two circuits are exactly the same. In the case of the measurements, the results are acceptably close. Note that the predicted gain for  $V_{DD} = 40$  mV is unity, thus for  $V_{DD} < 40$  mV the maximum absolute voltage gain is less than 1, disabling regeneration. The values for  $V_{DD} \geq 100$  mV are not included since hysteresis appears, and these circuits are meant to work as the amplifier of a Pierce oscillator exhibiting no hysteresis.

Figure 11b shows the simulation results for the maximum absolute gain over temperature. Since the gain decreases with increasing temperature to well below 2 V/V for a 60 mV supply, the measurement of the frequency of the oscillators as a function of the temperature was taken using a 90 mV supply, in order to arrive at insightful conclusions. These simulations predicted a slightly higher maximum absolute gain for circuit A compared with circuit B, in agreement with the simulation results reported in Fig. 11a. This effect becomes more relevant for low temperatures and  $V_{DD} = 90$  mV.

## V. MEASUREMENT RESULTS FOR THE CRYSTAL OSCILLATORS

Two PCBs were built in order to fully test both oscillators, one of which is based on circuit A and the other on circuit B. The values for the parameters of the crystals, the external capacitances and the feedback resistors, are reported in Table I.

A buffering stage is also included in the PCB and connected at the output using a TL072 operational amplifier, which has a very low input capacitance, to avoid excessively loading the oscillator. The actual capacitors connected to the crystal, the parasitic capacitances and the buffering stage input capacitances must add up to the design values of  $C_1$  and  $C_2$ , in order to properly tune the oscillation frequency. Unfortunately, the parasitic capacitances within oscillator A are too large, exceeding the total capacitance needed. As a consequence, the frequency of oscillator A was lower than the nominal

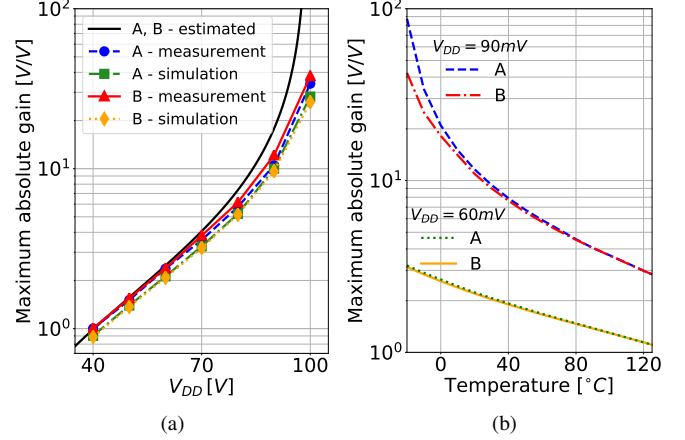


Fig. 11. Maximum absolute gain of the Schmitt trigger for circuits A and B, showing their dependence on (a) the supply voltage (simulations and measurements) and (b) the temperature (simulations only). For  $V_{DD} \geq 100$  mV hysteresis appears, and the circuits no longer work as amplifiers.

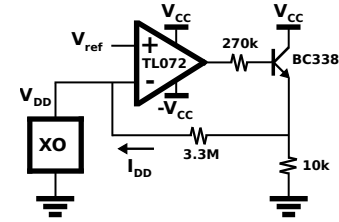


Fig. 12. Schematic of the auxiliary circuit used for current measurements.

resonance frequency of the crystal, which implies a poorer frequency stability. This and other consequences are fully explained in the rest of the paper and their impact on the performance parameters is quantified. In the case of oscillator B, the oscillation frequency was finely trimmed to the nominal frequency.

The measurement setup includes two DC voltage sources (HP 3245A, Tektronix PS280) to supply the oscillator and the buffering stage, respectively, an oscilloscope (Tektronix 1001B), a multimeter (Fluke 8846A). Also, another multimeter (Fluke 289) was used to measure temperature.

The current delivered to each of the oscillators was measured using a simple auxiliary current-to-voltage converter circuit [17] shown in Fig. 12. The results for oscillators A and B are given in Figs. 13a and 13b, respectively. It can be seen that the current and power consumption increase exponentially with the supply voltage, as expected for WI operation. However, the results for oscillator B deserve further inspection, since the measurement results are not very well predicted by the simulations. To this aim, Monte Carlo simulation results for the current consumption are shown in Figs. 14a and 14b for both oscillators with 60 mV and 90 mV supplies, respectively. It is seen that oscillator B measured current falls far from the distribution mean value, in agreement with the results presented in Fig. 13b. Consistently with results shown in Fig. 13a, oscillator A exhibits a measured current closer to the mean value of the distribution.

The variations of the drain currents of the transistors over



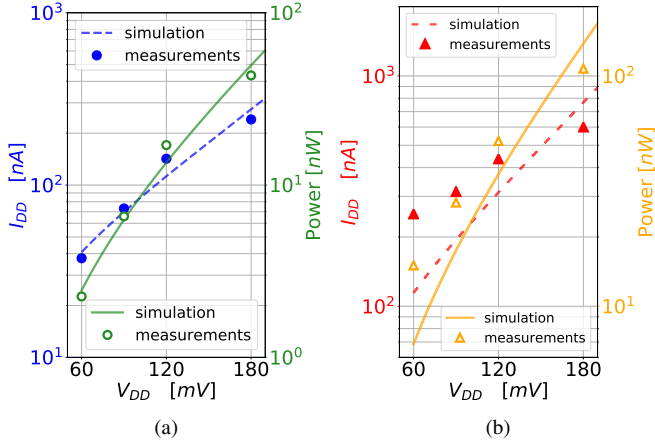


Fig. 13. Simulation and measurement results for the oscillators (a) A and (b) B, DC current and power consumption versus the supply voltage.

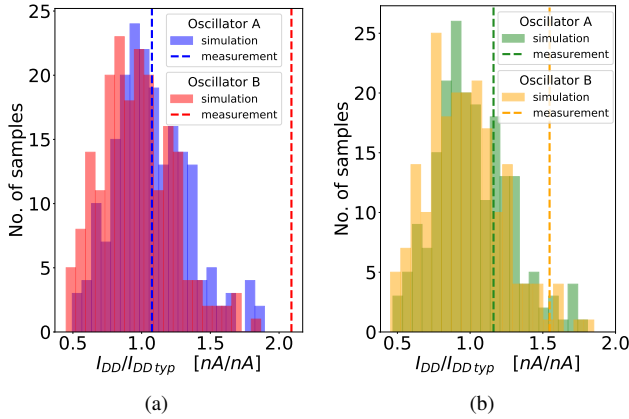


Fig. 14. Monte Carlo simulation and measurement results for the normalized current consumption of oscillators A and B for (a) 60 mV and (b) 90 mV supplies. The Monte Carlo simulations were run for 200 samples to obtain data for both the mismatch and the process variation.

temperature, as well as the total current consumption over temperature, were simulated. The results are shown in Figs. 15a and 15b, for oscillators A and B, respectively. All the currents are normalized to their typical value at 25°C. The results for the total current consumption  $I_{DD}$  in the worst case corner, FF, are also shown. In this corner, oscillator A starts-up only in the range from -10 to 100°C, while oscillator B starts-up in the whole considered temperature range.

#### A. Oscillator start-up

Figures 16a and 16b show the start-up transient measurements for oscillators A and B, respectively, for a supply voltage of 60 mV. The start-up time was measured for both oscillators with different values of the supply voltage  $V_{DD}$ , and the results are shown in Fig. 17a.

In order to determine the minimum supply voltage for which the oscillator starts up, measurements for eight samples were taken and the results are plotted in Fig. 17. It can be seen that all oscillators start up and that this occurs for supply voltages below 60 mV. Oscillator B starts-up at a lower supply voltage

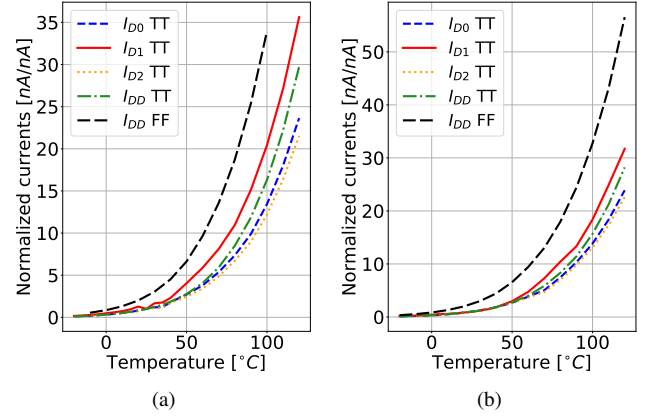


Fig. 15. Simulation results for the oscillators (a) A and (b) B, DC currents in steady state over temperature.  $I_{D0}$ ,  $I_{D1}$  and  $I_{D2}$  are the drain current of transistors  $M_{N0}$ ,  $M_{N1}$  and  $M_{N2}$ , respectively, normalized to the value at 25°C and 60 mV supply.  $I_{DD}$  is the current consumption of the oscillator in the TT and the FF corners, normalized to the value at 25°C and 60 mV supply in the TT corner

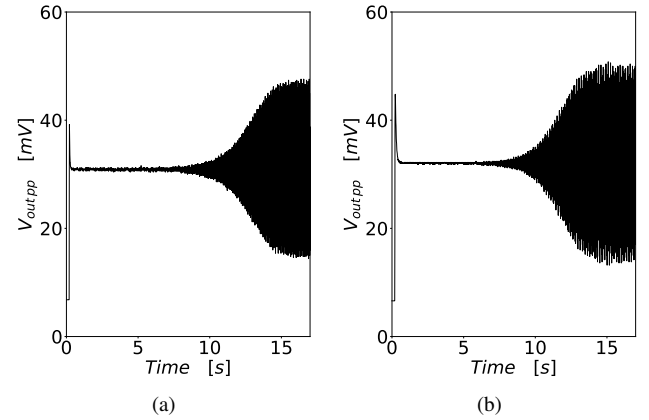


Fig. 16. Start-up of oscillators (a) A and (b) B, with 60 mV supply.

than oscillator A, which is consistent with the fact that circuit B exhibits a higher maximum absolute gain than circuit A, according to the results shown in Fig. 11a.

The minimum supply voltage varies over temperature, giving a minimum supply to start of 80 mV and 75 mV for oscillators A and B, respectively, at the upper limit of the temperature range measured (62°C).

#### B. Oscillator output voltage amplitude

The output voltage amplitude of oscillators A and B at resonance frequency was simulated through Monte Carlo simulations of the mismatch and process variation. The results are presented in Figs. 18a and 18b for supply voltages of 60 mV and 90 mV, respectively. Oscillation takes place with a yield of 100%, even though for a 60 mV supply the output signal could attain a peak to peak amplitude as small as 3 mV in some cases. Statistically, there is 5% probability that a sample of oscillator A exhibits a peak to peak output voltage smaller than 10 mV and in the case of oscillator B the probability is 9%. As seen in Fig. 18b, this effect decreases for a larger

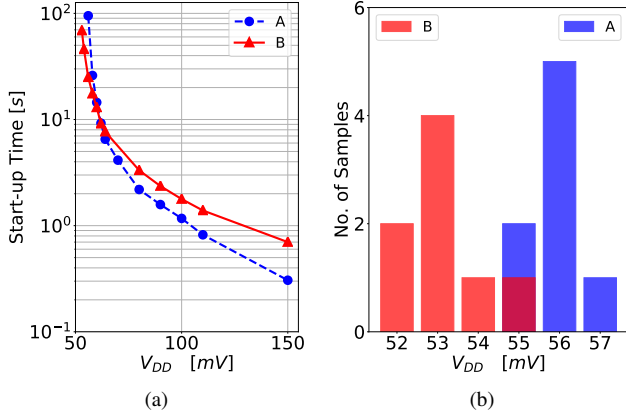


Fig. 17. Measurement results for oscillators A and B: (a) start-up time versus supply voltage and (b) minimum supply voltage for starting up. The start-up time was measured from the instant the DC output voltage reached 90 % of its final value until the instant when the amplitude of the oscillating signal was 90 % of its value at steady state.

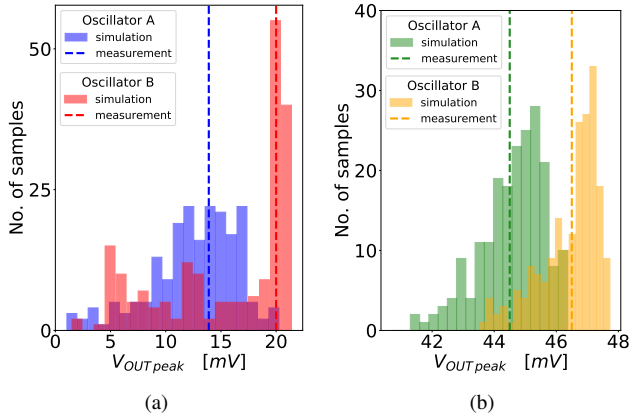


Fig. 18. Monte Carlo simulation and measurement results for the amplitude of the output voltage of oscillators A and B for (a) 60 mV and (b) 90 mV supplies. The Monte Carlo simulations were run for 200 samples to obtain data on both the mismatch and the process variation.

supply voltage, where all oscillator A samples attain at least a 39 mV peak and oscillator B samples at least a 36 mV peak.

Figure 19 shows the waveforms for the two oscillators with different supply voltages. The blue discontinuous line corresponds to oscillator A and the red continuous line, to oscillator B. For  $V_{DD} = 120$  mV and 180 mV the output waveform is visibly no longer sinusoidal. Furthermore, the harmonic components increase with the supply voltage. It should be noted that for  $V_{DD} = 110$  mV and above the Schmitt trigger exhibits hysteresis and loses the purely amplifying characteristic.

### C. Oscillator frequency

The frequency of the oscillators was measured, by means of a frequency counter (Agilent 53230A) linked to a time source (Symmetricom 5071A primary cesium frequency standard). The measurement results for the two oscillators are shown in Fig. 20a. The fractional frequency was normalized to the frequency obtained with a 60 mV supply. For oscillators A

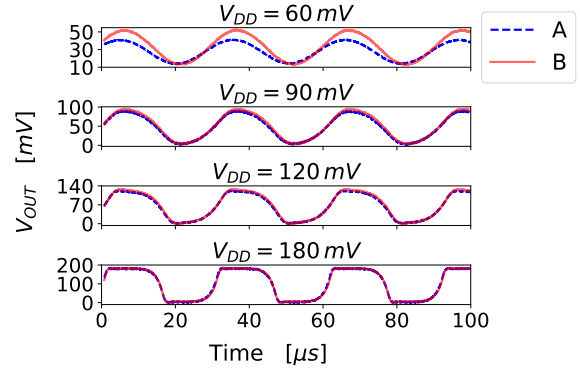


Fig. 19. Measurement results for the output voltage with different supply voltages,  $V_{DD}$ , for oscillators A and B.

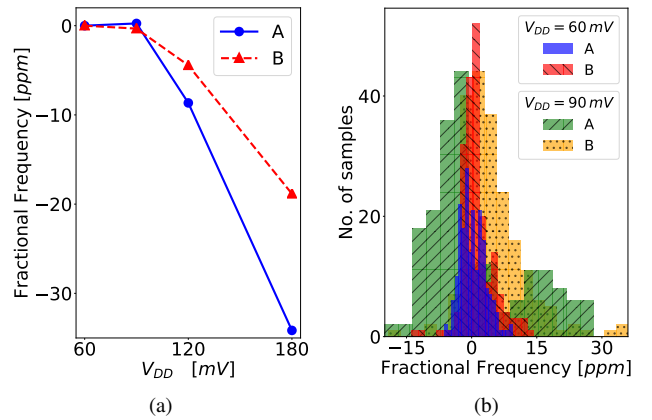


Fig. 20. (a) Measurement results for the fractional frequency normalized to that obtained with a 60 mV supply for oscillators A and B, and its dependence on the supply voltage. (b) Monte Carlo simulation results for the normalized fractional frequency for oscillators A and B, with either 60 mV or 90 mV supply. Simulations were run for 200 samples to obtain both mismatch and process variation.

and B, the fractional frequency varies only 0.251 ppm and 0.328 ppm, within the range from 60 mV to 90 mV supply, respectively. As a consequence, the fractional frequency has little dependence on the supply voltage within the range of interest where there is no hysteresis. As the hysteresis appears the frequency drops.

For reference purposes, the Monte Carlo simulation results are shown in Fig. 20b, where the normalized fractional frequency can be observed for both oscillators for supply voltages of 60 mV and 90 mV.

Fig. 21 shows the measurement results for the frequency stability for both oscillators operating with a 90 mV supply. Even though the temperature setup used allows for accurate temperature setting and measurement, the heating capability is limited to 62°C. Thus, the temperature was ramped from ambient temperature to 62°C within 4 h and back to ambient temperature over another 4 h, and the frequency was measured at a rate of once per second, obtaining as a result the shaded area in which the actual frequency stability falls. The same procedure was carried out to obtain measurements below ambient temperature. The curves for the typical values of the intrinsic instability of the used crystal resonators are super-

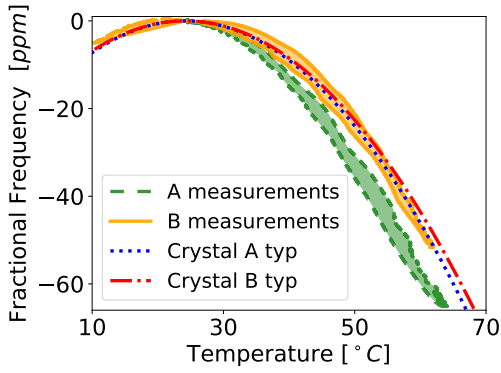


Fig. 21. Measurement results for the fractional frequency normalized to that obtained at 26°C for circuits A and B with 90 mV supply, and its dependence on temperature compared to typical values of the intrinsic instability of the used crystal resonators (provided in the datasheets).

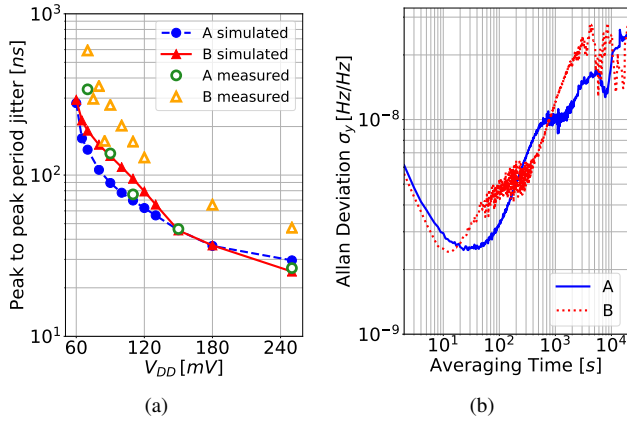


Fig. 22. Results for the oscillator performance: (a) simulation and measurement results for time jitter versus supply voltage, and (b) Allan deviation measurements with a supply voltage  $V_{DD} = 60$  mV.

imposed for reference. The frequency stability of oscillator B falls within the crystal specifications, indicating that the stability is not altered by the presence of circuit B. In the range of 5–62°C, a stability of 50 ppm is attained. On the other hand, oscillator A exhibits less frequency stability, as expected, due to the poor frequency trimming. In this case, the stability is 62 ppm within the range of 25–62°C.

Time jitter was measured using a digital oscilloscope (Tektronix MSO5204). Peak to peak jitter measurements of oscillators A and B are shown next to simulation results in Fig. 22a. As the supply voltage increases the jitter decreases, as expected.

Measurement results of the Allan deviation for both oscillators are shown in Fig. 22. The measurements were taken with an averaging time of 1 s over 10 h, with a maximum temperature variation of 0.5°C. It can be seen that the Allan deviation is below 30 ppb for both oscillators.

#### D. Comparison to other works

Table III summarizes the details for state-of-the-art ultra-low-voltage crystal oscillators of frequency 32 kHz and compares these to the results of this study.

To the best of the authors knowledge, the oscillators presented herein are the crystal oscillators for 32 kHz with the lowest operating voltage, working with only 60 mV. The closest prior works in terms of low supply voltage are [21] and [18]. [21] reports a minimum supply voltage of 100 mV in part of oscillator circuit, but requires also a second, higher, supply voltage, from 400 mV on. [18] operates down to 150 mV with a supply voltage drift well above all other reported values, remarkable power consumption, temperature stability and Allan deviation. The power consumption reduction is traded-off with a modification in the oscillator output waveform, which might degrade the frequency spectrum. Furthermore, it needs a conventional crystal oscillator to start-up, requiring more area.

The power consumption of oscillator A is very well suited for ultra-low-power applications and in line with other state-of-the-art oscillators. Prior works with comparable ultra-low-power consumption are [24], [19], [18] and [21]. The drawbacks of [18] and [21] have already been discussed. In [24], a power consumption of 0.55 nW is achieved by means of downconverting the signal to DC, amplifying in DC and then upconverting the signal to the frequency of the crystal. An excellent phase synchronization is achieved providing excellent frequency stability over temperature and over time. The output waveform is the result of switching DC levels to obtain a four level switched signal, which will have important harmonic content. The output harmonic content would be filtered by the high quality factor of the crystal. Nevertheless, this might be an issue if spectral purity is needed. [19] reaches a minimum supply voltage of 300 mV while decreasing consumption by means of a sophisticated duty-cycling mechanism. However, a large silicon area is required and the Allan deviation is much larger than that attained in the present work. In order to further reduce the power consumption of a Schmitt trigger-based crystal oscillator, the parasitic capacitances should be lowered using smaller packaging rather than DIP40. Furthermore, a crystal specified for a lower load capacitance would reduce the power consumption. Reduction in packaging capacitances also allows a better tuning of the oscillator frequency in the case of oscillator A.

The approach described herein is also notable for the extremely small silicon area budget, using standard CMOS transistors within a widely used and inexpensive technology. This small area is due to the use of a standalone amplifier, with no calibration or auxiliary circuits needed to improve the power consumption or frequency stability. Other designs shown in Table III are several times bigger, even those in more advanced technology nodes.

Performance aspects, where other designs in Table III are better than this work, are start-up time ([21], [23]) and Allan deviation ([18], [21], which drawbacks were previously discussed). Regarding start-up time, [21] and [23] require much higher minimum operating voltage. Furthermore, the start-up time and the Allan deviation in the designs here presented are still within the range achieved or better than other state-of-the-art works, as visible in Table III.

Summing up, the designs shown in this work, provide record low operating voltage and a very compact implementation



TABLE III  
COMPARISON TO PRIOR WORK

	[10]	[18]	[19]	[20]	[21]	[22]	[23]	[24]	This work	
									A	B
Technology	2 $\mu\text{m}$	28 nm	0.13 $\mu\text{m}$	0.18 $\mu\text{m}$	55 nm	40 nm	0.18 $\mu\text{m}$	65 nm	0.13 $\mu\text{m}$	0.13 $\mu\text{m}$
Area ( $\text{mm}^2$ )	N/A	0.03	0.0625	0.027	0.16	0.07	0.035	0.027	0.0033	0.0065
Frequency (kHz)	32.8	32.768	32.768	32.768	32.768	32.76	32.768	32	32.763	32.768
Crystal total load capacitance (pF)	8.2	N/A	3	N/A	N/A	N/A	2.23	7.5	3	12.5
Supply voltage (V)	0.71 - 1.7	0.15 - 0.5	0.3 - 0.9	0.25 - 0.5	0.1 - 0.5 0.4 - 0.8	0.5	0.4 - 5.5	0.5	0.06 - 0.1	0.06 - 0.1
Supply voltage drift (ppm/V)	N/A	$\sim 83$	7	N/A	6.7	1	2.1	13	8.4	11
Power consumption (nW)	23	1.89	1.5	2.89	1.7	47	10 nW@1V	0.55	2.26	15.0
Amplitude of oscillation (mV)	130	150	230	250	100	N/A	90	500	27.5	40
Start-up time	N/A	N/A	31 s	N/A	8 ms	N/A	1 ms	0.2 s	14.5 s	13.0 s
Temperature stability	N/A	48.8 ppm -20 $\sim$ 80 $^\circ\text{C}$	-150 ppm 0 $\sim$ 80 $^\circ\text{C}$	N/A	109.1 ppm -20 $\sim$ 80 $^\circ\text{C}$	0.25 ppm/ $^\circ\text{C}$ @room temp	120 ppm -40 $\sim$ 85 $^\circ\text{C}$	80 ppm -20 $\sim$ 80 $^\circ\text{C}$	-62 ppm 25 $\sim$ 62 $^\circ\text{C}$	-50 ppm 5 $\sim$ 62 $^\circ\text{C}$
Allan deviation	N/A	$\sim 2$ ppb	90 ppb	N/A	2.5 ppb	N/A	N/A	14 ppb	30 ppb	30 ppb

The crystal oscillator in [21] is PLL-assisted and requires two different supply voltages. The two operating ranges are reported. Crystal total load capacitance is the series of  $C_1$  and  $C_2$ , including parasitic capacitances. Amplitude of oscillation is peak to peak. Amplitude of oscillation and power consumption are reported at the lowest operating supply voltage. Unless stated otherwise, results are reported at room temperature.

with competitive consumption and precision specifications (temperature stability, long term stability, supply voltage drift).

## VI. CONCLUSION

The design, simulation and measurement results for two crystal oscillators are presented herein. They are based on the application of a Schmitt trigger as an amplifier. Guidelines for designing this block to be the amplifier of a crystal oscillator are provided. The amplifiers A and B were experimentally characterized, providing a gain of 2.48 V/V with a 60 mV power supply. The oscillators operate with the lowest reported supply voltage of only 60 mV while providing temperature and long-term stability competitive with respect to state-of-the-art ultra-low-voltage crystal oscillators. Oscillator A exhibits a power consumption in line with the best state-of-the-art oscillators previously reported.

### APPENDIX A

#### PIERCE CRYSTAL OSCILLATOR OPERATION

The impedance  $Z_C$  shown in Fig. 6b can be expressed as [11]

$$Z_C = \frac{Z_1 Z_3 + Z_2 Z_3 + G_m Z_1 Z_2 Z_3}{Z_1 + Z_2 + Z_3 + G_m Z_1 Z_2}, \quad (7)$$

where  $Z_1$ ,  $Z_2$  and  $Z_3$  are the impedances of capacitors  $C_1$ ,  $C_2$  and  $C_3$ , respectively. The imaginary part of  $Z_C$  is negative, since it is a purely capacitive impedance. The real part of  $Z_C$  is negative, provided that  $G_m$  has positive values, and is equal to  $-R_m$  when the critical condition for oscillation is reached at  $G_{m\text{crit}}$

$$G_{m\text{crit}} = \omega^2 C_1 C_2 R_m \left( 1 + \frac{C_3}{C_1} + \frac{C_3}{C_2} \right)^2. \quad (8)$$

Equation (8) is valid as long as [11]

$$2\omega R_m C_3 (1 + C_3/C_1 + C_3/C_2) \ll 1. \quad (9)$$

It will be verified that the design complies with this condition.

On the other hand,  $G_{m\text{opt}}$  is the transconductance value required to achieve the maximum negative resistance possible, and is given by

$$G_{m\text{opt}} = \omega \left( C_1 + C_2 + \frac{C_1 C_2}{C_3} \right). \quad (10)$$

It will be verified that even though  $G_m = 3 \times G_{m\text{crit}}$ , it is smaller than  $G_{m\text{opt}}$ . The determination of  $G_m$  must also compensate the losses in the inverting amplifier. These losses are not negligible at low supply voltages.

The real part of  $Z_C$ ,  $R_C$ , increases by the amount  $\Delta R_C$  due to the losses in  $G_o$

$$\Delta R_C = \frac{G_o}{(\omega C_2)^2 \left( 1 + \frac{C_3}{C_1} + \frac{C_3}{C_2} \right)^2}. \quad (11)$$

Assuming small losses,  $G_o \ll \omega C_2$ , and based on (8) and (11), the increase in  $G_{m\text{crit}}$  needed to compensate  $G_o$  is

$$\Delta G_m = \frac{C_1}{C_2} G_o. \quad (12)$$

### APPENDIX B

#### TRANSCONDUCTANCES OF THE SCHMITT TRIGGER

The expressions for the equivalent transconductance and the output conductance of the Schmitt trigger are [13]

$$G_m = \left. \frac{i_o}{v_i} \right|_{V_i=V_o=V_{DD}/2} \quad (13)$$

$$= -2 \times \frac{g_{m1}(g_{ms2} + g_{md0}) + g_{ms1}g_{m0}}{g_{ms1} + g_{ms2} + g_{md0}},$$

and

$$G_o = \left. \frac{i_o}{v_o} \right|_{V_i=V_o=V_{DD}/2} \quad (14)$$

$$= -2 \times \frac{g_{md1}(g_{ms2} + g_{md0}) - g_{ms1}g_{m2}}{g_{ms1} + g_{ms2} + g_{md0}}.$$

where the transconductances are given in Table I of [15] and the subscript number correspond to the transistor number in Fig. 1.

The equivalent transconductance  $G_m$  can be rewritten in terms of the supply voltage,  $V_{DD}$ , and the current strengths,  $I_0$ ,  $I_1$  and  $I_2$ , as follows

$$G_m = \frac{2I_1/n}{e^{-V_{DD}/2n\phi_t}} \left[ \frac{(I_0 + I_2)e^{-V_{DD}/2\phi_t} - I_2e^{-V_{X0}/\phi_t}}{I_0 e^{(V_{X0}-V_{DD})/\phi_t} + I_1 + I_2} \right], \quad (15)$$

where

$$e^{-V_{X0}/\phi_t} = \frac{I_0 + I_1e^{-V_{DD}/2\phi_t} + I_2e^{-V_{DD}/\phi_t}}{I_0 + I_1 + I_2}. \quad (16)$$

#### ACKNOWLEDGMENT

The authors would like to acknowledge the support from grant ANII POS\_NAC\_2015\_1\_109743, CAP and CSIC Universidad de la República, the project STIC AmSud O2ERF and the Brazilian research agency Coordenação de Aperfeiçoamento de Pessoal de Nível Superior (CAPES), Finance Code 001, along with MOSIS for providing access to integration. We are grateful to the director of the Laboratory of UTE, Uruguay, Daniel Slomowitz, and members of his staff for making themselves and their equipment available for the high precision frequency measurements.

#### REFERENCES

- [1] D. Yoon, T. Jang, D. Sylvester, and D. Blaauw, "A 5.58 nW crystal oscillator using pulsed driver for real-time clocks," *IEEE Journal of Solid-State Circuits*, vol. 51, no. 2, pp. 509–522, Feb 2016.
- [2] C. J. Love, S. Zhang, and A. Mershin, "Source of sustained voltage difference between the xylem of a potted ficus benjamina tree and its soil," *PLoS ONE*, vol. 3, no. 8, e2963, 2008.
- [3] P. Weng, H. Tang, P. Ku, and L. Lu, "50 mV-input batteryless boost converter for thermal energy harvesting," *IEEE Journal of Solid-State Circuits*, vol. 48, no. 4, pp. 1031–1041, April 2013.
- [4] S. Bandyopadhyay, P. P. Mercier, A. C. Lysaght, K. M. Stankovic, and A. P. Chandrakasan, "A 1.1 nW energy-harvesting system with 544 pW quiescent power for next-generation implants," *IEEE Journal of Solid-State Circuits*, vol. 49, no. 12, pp. 2812–2824, Dec 2014.
- [5] N. Lotze and Y. Manoli, "A 62 mV 0.13 $\mu$ m CMOS standard-cell-based design technique using Schmitt-trigger logic," *IEEE Journal of Solid-State Circuits*, vol. 47, no. 1, pp. 47–60, Jan 2012.
- [6] —, "Ultra-sub-threshold operation of always-on digital circuits for IoT applications by use of Schmitt trigger gates," *IEEE Transactions on Circuits and Systems I: Regular Papers*, vol. 64, no. 11, pp. 2920–2933, Nov 2017.
- [7] R. G. Dreslinski, M. Wiecekowsk, D. Blaauw, D. Sylvester, and T. Mudge, "Near-threshold computing: Reclaiming Moore's law through energy efficient integrated circuits," *Proceedings of the IEEE*, vol. 98, no. 2, pp. 253–266, Feb 2010.

- [8] A. Bryant, J. Brown, P. Cottrell, M. Ketchen, J. Ellis-Monaghan, and E. J. Nowak, "Low-power CMOS at  $V_{dd} = 4kT/q$ ," in *Device Research Conference. Conference Digest (Cat. No.01TH8561)*, June 2001, pp. 22–23.
- [9] J. Choi, E. Aklimi, C. Shi, D. Tsai, H. Krishnaswamy, and K. L. Shepard, "Matching the power, voltage, and size of biological systems: A nW-scale, 0.023-mm<sup>3</sup>pulsed 33-GHz radio transmitter operating from a 5 kT/q-supply voltage," *IEEE Transactions on Circuits and Systems I: Regular Papers*, vol. 62, no. 8, pp. 1950–1958, Aug 2015.
- [10] W. Thommen, "An improved low power crystal oscillator," in *Proceedings of the 25th European Solid-State Circuits Conference*, Sep. 1999, pp. 146–149.
- [11] E. Vittoz, *Low-Power Crystal and MEMS Oscillators: The Experience of Watch Developments*. Springer, 2010.
- [12] M. Toki, "Low DC-driving-voltage crystal oscillator," in *Proceedings of the 1999 Joint Meeting of the European Frequency and Time Forum and the IEEE International Frequency Control Symposium (Cat. No.99CH36313)*, vol. 1, April 1999, pp. 412–415 vol.1.
- [13] L. A. P. Melek, M. C. Schneider, and C. Galup-Montoro, "Operation of the classical CMOS Schmitt trigger as an ultra-low-voltage amplifier," *IEEE Transactions on Circuits and Systems II: Express Briefs*, vol. 65, no. 9, pp. 1239–1243, Sep. 2018.
- [14] M. C. Schneider and C. Galup-Montoro, *CMOS Analog Design Using All-Region MOSFET Modeling*. Cambridge University Press, 2010.
- [15] L. A. P. Melek, A. L. da Silva, M. C. Schneider, and C. Galup-Montoro, "Analysis and Design of the Classical CMOS Schmitt Trigger in Subthreshold Operation," *IEEE Transactions on Circuits and Systems I: Regular Papers*, vol. 64, no. 4, pp. 869–878, April 2017.
- [16] R. M. Cerda, *Understanding Quartz Crystals and Oscillators*. Artech House, 2014.
- [17] M. A. Al-Qutayri, W. J. Tenten, and P. R. Shepherd, "A prototype supply current monitor for testing analogue circuits," in *Proceedings. Tenth Annual IEEE International ASIC Conference and Exhibit (Cat. No.97TH8334)*, Sep. 1997, pp. 38–41.
- [18] K. Hsiao, "17.7 a 1.89 nW/0.15 V self-charged XO for real-time clock generation," in *2014 IEEE International Solid-State Circuits Conference Digest of Technical Papers (ISSCC)*, Feb 2014, pp. 298–299.
- [19] A. Shrivastava, D. Akella Kamakshi, and B. H. Calhoun, "A 1.5 nW, 32.768 kHz XTAL oscillator operational from a 0.3 V supply," *IEEE Journal of Solid-State Circuits*, vol. 51, no. 3, pp. 686–696, March 2016.
- [20] S. Wu and T. Lee, "Ultra-low-power one-pin crystal oscillator with self-charged technique," *Electronics Letters*, vol. 52, no. 4, pp. 325–327, 2016.
- [21] Y. Zeng, T. Jang, Q. Dong, M. Saligane, D. Sylvester, and D. Blaauw, "A 1.7 nW PLL-assisted current injected 32 kHz crystal oscillator for IoT," in *2017 Symposium on VLSI Circuits*, June 2017, pp. C68–C69.
- [22] A. Lahiri, P. Badrathwal, N. Jain, and K. Chatterjee, "A 0.5 V supply, 49 nW band-gap reference and crystal oscillator in 40 nm CMOS," in *2017 IEEE Custom Integrated Circuits Conference (CICC)*, April 2017, pp. 1–4.
- [23] M. Coustans, F. Krummenacher, M. Kayal, L. Rossi, M. Dellea, Y. Godat, Y. Sierro, and S. DallaPiazza, "A 32 kHz crystal oscillator leveraging voltage scaling in an ultra-low power 40 nA real-time clock," in *2018 31st IEEE International System-on-Chip Conference (SOCC)*, Sep. 2018, pp. 308–313.
- [24] H. Esmaeelzadeh and S. Pamarti, "18.4 a 0.55nW/0.5V 32kHz crystal oscillator based on a DC-only sustaining amplifier for IoT," in *2019 IEEE International Solid-State Circuits Conference - (ISSCC)*, Feb 2019, pp. 300–301.



**Mariana Siniscalchi** (S'16) received the Electronics Engineering degree from Universidad de la República, Uruguay, in 2014. She is currently pursuing a Ph.D. in Electrical Engineering at Universidad de la República, where she is an Assistant Professor. Her research interests are related to ultra-low-voltage and ultra-low-power applications and transistor level design of both analog and digital circuits, in particular crystal oscillators and LC oscillators. She is also interested in applications regarding wireless sensor networks and temperature sensors.



**Fernando Silveira** (S'88–M'91–SM'03) received the Electrical Engineering degree from the Universidad de la República, Uruguay, in 1990, and the M.Sc. and Ph.D. degrees in microelectronics from the Université catholique de Louvain, Belgium, in 1995 and 2002, respectively. He has had multiple industrial activities, including leading the design of an ASIC for implantable pacemakers and designing analog circuit modules for implantable devices for various companies worldwide. He is currently a Professor with the Electrical Engineering Department,

Universidad de la República. His research interests include the design of ultra-low-power analog and RF integrated circuits and systems, in particular with biomedical application. In this field, he has co-authored a book and many technical articles.



**Carlos Galup-Montoro** (M'89,SM'17) studied Engineering Sciences at the University of the Republic, Montevideo, Uruguay, and Electronic Engineering at the National Polytechnic School of Grenoble (INPG), France. He received an Engineering degree in electronics in 1979 and a doctorate degree in 1982, both from INPG.

From 1982 to 1989 he worked at the University of São Paulo, Brazil. Since 1990 he has been with the Electrical Engineering Department, Federal University of Santa Catarina, Florianópolis, Brazil, where

he is now a Professor. In the second semester of the academic year 1997/98 he was a research associate with the Analog Mixed Signal Group, Texas A&M University. He was a visiting scholar at UC Berkeley in the academic year 2008/09 and at IMEP/INPG in the first trimester of 2017.